

# Quantum limited optical phase detection at the $10^{-10}$ radian level

Brian Lantz <sup>1</sup>, Peter Fritschel, Haisheng Rong <sup>2</sup>, Ed Daw <sup>3</sup>

Department of Physics and Center for Space Research, Massachusetts  
Institute of Technology, Cambridge, MA 02139

Gabriela González

Department of Physics, The Pennsylvania State University, University  
Park, PA 16802

February 20, 2001

submitted to JOSA A

LIGO-P000023-02-D

Interferometric detection of gravitational waves at a level of astrophysical interest is expected to require measurement of optical phase differences of  $\leq 10^{-10}$  rad. A fundamental limit to the phase sensing is the statistics of photon detection—Poisson statistics for light in a coherent state. We have built a laboratory-scale interferometer to achieve and investigate the phase detection sensitivity required for the Laser Interferometer Gravitational-Wave Observatory (LIGO). With 70 W of circulating power, we have obtained a phase sensitivity of  $1.28 \times 10^{-10}$  rad/ $\sqrt{\text{Hz}}$  at frequencies above 600 Hz, limited by quantum noise. Below 600 Hz, excess noise above the quantum limit is seen, and we present our investigations into the sources of this excess. Compared to previous such experiments, we have improved the phase sensitivity over the full 100 Hz-10 kHz band of interest by factors of up to 100, with a factor of 2.5 improvement in the quantum-limited level.

© 2001 Optical Society of America

**OCIS codes:** 270.5290, 120.2230, 120.3180, 120.5050

---

<sup>1</sup>current address: Ginzton Lab, Stanford University, Palo Alto, CA, 94040

<sup>2</sup>current address: New Focus, Inc., Santa Clara, CA 95051

<sup>3</sup>current address: Department of Physics, Louisiana State University, Baton Rouge, LA

## 1. Introduction

According to Einstein’s theory of general relativity, gravitational waves exist as oscillations in the space-time metric, radiated by accelerating aspherical mass distributions. An interferometric gravitational wave detector attempts to measure these oscillations capitalizing on the apparent change in light travel time induced by the gravitational wave: two light beams are directed to probe separate space-time paths and then are interfered; travel time differences between the two paths produce optical phase differences which are detectable as light intensity changes[1]. A Michelson interferometer with orthogonal arms is used because its geometry is well-matched to the space-time distortion of the effect—during any half-cycle of the oscillation, the quadrupolar gravitational-wave field increases the travel time in one arm and decreases it in the other arm[2]. A Sagnac interferometer can also be used[3]; in this case the two counter-propagating beams travel the same path, but at different times (one path is the time-reversed of the other), and a net travel time difference is produced by gravitational-wave periods of order the interferometer round trip time.

Regardless of the specific configuration of an interferometer, it must be extremely sensitive to the optical phase difference between its paths to achieve a meaningful gravitational wave sensitivity. Since the (dimensionless) gravitational wave produces the equivalent of a strain in space, the instrument sensitivity is described in terms of a strain sensitivity. The large-scale interferometer projects currently under construction by LIGO[4], VIRGO[5], GEO[6] and TAMA[7] all have target sensitivities in the range of  $10^{-21}$  in strain (change in length per unit length). Numerous variants of the basic Michelson and Sagnac interferometer configurations have been designed to convert this gravitational-wave strain into optical phase difference in an efficient manner. The interferometers in LIGO, for example, contain a 4-km-long resonant Fabry-Perot cavity in each arm of a Michelson; these storage cavities increase the interaction of the light beams with the gravitational-wave strain, building up the optical phase shift by a factor proportional to the cavity finesse. For this geometry, the optical phase difference  $\delta\phi$  produced by a gravitational-wave of amplitude  $h$  and frequency  $f$ , incident on the interferometer with optimal orientation, is

$$A(f) \equiv \left| \frac{\delta\phi(f)}{h(f)} \right| = \frac{8\pi\nu_l\tau_s}{\sqrt{1 + (4\pi f\tau_s)^2}} \quad (1)$$

where  $f$  is the gravitational-wave frequency,  $\nu_l$  is the laser frequency, and  $\tau_s$  is the energy decay time of the cavities; the last is related to the cavity finesse  $F$  by  $\tau_s = Fl/c\pi$ , where  $l$  is the cavity length. The storage time is chosen to optimize the strain sensitivity in the context of various unavoidable noise sources in the instrument. The LIGO cavities are illuminated

by 1064 nm-wavelength light, and they have a storage time of  $\tau_s = 0.9$  msec, giving a DC response of  $A(0) = 6.4 \times 10^{12}$  radians (per unit strain).

We can now estimate the optical phase sensitivity required to give a  $10^{-21}$  strain sensitivity. A gravitational-wave of frequency 150 Hz (where LIGOs sensitivity is best) and amplitude  $10^{-21}$  would produce an optical phase difference of  $\sim 3 \times 10^{-9}$  rad (again, assuming optimal orientation). The signal that this produces must be detectable in the presence of random noise also present at the output; shot-noise in the photodetection, for example, is one of the major contributors to the noise at 150 Hz. Assuming that the gravitational wave is a burst that might last for one to several cycles, the bandwidth of the signal is of order  $BW = 150$  Hz. The spectral density of the random noise, when expressed as an equivalent ‘phase noise’, then must be less than  $3 \times 10^{-9}/\sqrt{BW} \approx 3 \times 10^{-10}$  rad/ $\sqrt{\text{Hz}}$  by some factor which depends on the required signal-to-noise ratio for detection. The actual target phase sensitivity of a LIGO interferometer as a function of frequency is shown in 1; for frequencies  $f > 150$  Hz, the interferometers are designed to be quantum noise limited—as determined by the Poisson statistics of photon detection (‘shot’ noise).

We present in this paper the results of a laboratory scale Michelson interferometer designed to operate at or near the LIGO phase sensitivity. The main motivation for this work was to identify and control the technical sensing noise sources that compete with the quantum noise; we generally identify as ‘sensing’ noise sources those which do not directly affect the positions of the interferometer mirrors (as opposed to ‘displacement’ noise sources, such as seismic noise, which in some way produce accelerations of the mirrors; the distinction is not always so clean, however). To put the required level of phase sensitivity into context, we show in Figure 1 the results of this work along with three other interferometric optical phase measurements. In particular this paper is an extension of the work presented in reference [11] using a very similar interferometer design; compared to this previous work, we have improved the phase sensitivity over the full 100 Hz-10 kHz band of interest by factors of 2.5-100, with a factor of 2.5 improvement in the quantum-limited level. It should be noted that a complementary experiment has been performed to investigate the displacement sensitivity required for LIGO, and is described in reference[12].

## 2. Instrument Description

Figure 2 shows a simplified schematic, and Table I gives significant parameters of the system. The optical configuration includes a simple one-bounce Michelson interferometer. The Fabry-Perot arm cavities mentioned above are not included in this system; since the primary function of such storage cavities is to

increase the displacement sensitivity of an interferometer, they are not required for the phase sensitivity goals of this experiment, and we forego them to reduce the complexity of the system. The other aspects of the optical configuration are very similar to the LIGO design. To reduce sensitivity to fluctuations of the input laser power, the average Michelson arm length difference is controlled so that the intensity at the anti-symmetric or signal output is a minimum; at this point, the interferometer is said to be operating on a ‘dark fringe’, and almost all the input light is reflected back towards the laser. This allows the use of a ‘power recycling’ technique[13][14], in which a partially transmitting mirror is placed between the laser and the 50/50 beam splitter, forming an optical cavity between this power-recycling mirror and the symmetric port of the Michelson. When the position of the recycling mirror is properly controlled, the cavity is resonant with the incident light, the power incident on the beamsplitter builds up, and (for the proper choice of recycling mirror transmission) almost no power is reflected back towards the laser. The increase in effective laser power—by a factor  $G_{rec}$  known as the power-recycling gain—improves the shot noise-limited sensitivity of the interferometer by a factor of  $\sqrt{G_{rec}}$ . The remaining significant feature of the interferometer configuration is the fact that it is intentionally operated with unequal arm lengths[15]. This is done as part of the signal or phase sensing system, described in detail below.

The interferometer is illuminated with a single-frequency diode-pumped Nd:YAG laser, emitting 700 mW at 1064 nm (Lightwave Electronics model 126-1064-700). Superb frequency stability is required to reach the desired level of phase sensitivity, and a two-stage frequency stabilization scheme has been implemented to achieve this. The first prestabilization stage uses a fixed-spacer reference cavity to define the laser frequency; a feedback control system makes the laser frequency track a cavity resonance. The second stage wraps this system in another feedback system for further suppression of residual fluctuations, this time using the suspended interferometer as a low-noise reference.

For the laser prestabilization[16], 20 mW is split off from the main beam and sent to the reference cavity, consisting of a cylindrical fused silica spacer with mirrors optically contacted to each end; the FWHM linewidth of the cavity is 75 kHz. Isolation from vibrations is provided by a three layer steel plate and elastomer stack, and by mounting the cavity on top of this stack with two short wire loops, one near each end; the cavity and isolation system are contained in a  $10^{-8}$  torr vacuum vessel.

The Pound-Drever-Hall reflection locking technique[17] is used to generate the error signal for locking the laser to the cavity. The error signal—proportional to the difference between the laser frequency

and the cavity resonance—is amplified, filtered, and fed back to three actuators to control the frequency of the main and sample beams. Two of the actuators are part of the laser: a thermal actuator which heats or cools the laser crystal to change the crystal dimensions, and a piezo-electric transducer (PZT) bonded to the laser crystal, which squeezes the crystal to change the lasing frequency. The third actuator is an externally mounted phase modulating Pockels cell. The thermal actuator has a slow response, but the largest range with a tuning coefficient of 4 GHz/Volt; it is used to bring the laser into resonance with the cavity and is adjusted when needed to null offsets in the PZT feedback path. The PZT has a flat frequency response to 100kHz and does the bulk of the frequency correction. The Pockels cell path becomes effective above 50kHz, and provides the fast response necessary to achieve a loop bandwidth of 1MHz.

Before coupling into the reference cavity, the sample beam makes a double-pass through an acousto-optic modulator (AOM), which serves as an actuator for the second stage of frequency stabilization. The AOM is driven with a voltage-controlled oscillator (VCO), operating at a center frequency of 80 MHz with a linear tuning range of  $\pm 5$  MHz. The center of the AOM is positioned at the center of curvature of the mirror that retro-reflects the beam for the second pass; this minimizes the beam direction change as the AOM drive frequency is varied. The sample beam is thus shifted by 150-170 MHz with respect to the main laser beam according to the VCO control input. This shift is also useful to spectrally isolate the prestabilization beam from the main beam.

The main laser beam passes through an electro-optic phase modulator, driven sinusoidally at  $f_m$  with a relatively small amplitude, such that only the carrier light, at frequency  $\nu_l$ , and the first order modulation sidebands, at  $\nu_l \pm f_m$ , have significant amplitude. These radio-frequency (rf) sidebands are used in a heterodyne detection system to sense the relative optic positions and angles, using variants of the Pound-Drever-Hall technique.

The interferometer optics are mounted on two seismically isolated platforms, one for the beamsplitter and arm mirrors, and one for the recycling mirror; the optics, the two platforms and the 6 m path between them are enclosed in high-vacuum. The three mirrors and beamsplitter are fused silica and have multilayer dielectric coatings to achieve a desired reflectivity. Each optic is suspended as a pendulum by a single loop of steel wire, and its position with respect to its suspension support structure is sensed with a small LED-based optical sensor. The position and orientation of each optic can be controlled via electromagnetic motors: five magnets are bonded to the optic (four on the back face and one on the side) and five coils are mounted on the support structure, concentric with the magnet axes and axially posi-

tioned such that the magnet experiences the largest magnetic field gradient. The sensor signals are used to actively damp four rigid-body modes—an axial and a transverse mode at 1 Hz, and two angular modes at 0.45 Hz—using the coils to provide the damping forces. The mounting platforms are seismically isolated in two stages: a commercial low-frequency active isolation system[18] (mounted outside the vacuum system on the floor) provides good isolation in the 2-20 Hz decade; a passive four-layer mass-spring stack[19] adds increasing isolation above 20 Hz, achieving a ground vibration transmission of  $10^{-6}$  at 100 Hz.

We also found that some level of environmental isolation of the input and output optics (i.e., all components outside the vacuum system) was crucial to reduce the effects of scattered light. The phenomenon here involves light that is scattered or otherwise back-reflected by elements in the optical chain, travels a different path than the main laser beam, and then recombines with the main beam. If this scattering path is modulated (seismically or acoustically), the relative phase between the main and scattered fields will be modulated, producing a spurious amplitude modulation in the signal[20]. For relative path motions greater than a wavelength, the relative phase changes by multiple  $\pi$ , and frequency upconverted components appear at the output up to frequencies of  $2v/\lambda$  (Hz), where  $v$  is the relative velocity of scattering path. When the relative motions are smaller than a wavelength, the coupling is approximately linear. In our experience, scattering in the input optics (all components between the laser and the recycling mirror) generally showed up through frequency upconversion, whereas scattering in the output optics generally produced linearly coupled noise. To reduce these effects on the input side, the laser table is mounted on another set of commercial active isolators so that relative motion between the laser source and the recycling mirror is less than a wavelength in the 1-10 Hz band. On the output side, the detection table is mounted on pneumatic passive isolators, and is surrounded by an acoustic isolation enclosure. The amount of backscattered light was reduced by using low micro-roughness mirrors in the output chain; the remaining scattered light was dominated by that from the photodiode surface [21].

### 3. Sensing and controls

To describe the operating point of the interferometer we define two macroscopic lengths,  $l_r$  and  $\Delta l$ , and two microscopic lengths,  $\delta l_r$  and  $\delta l_M$ ; the macroscopic lengths are assumed to exactly fulfill the resonance conditions, whereas the microscopic lengths denote small variations (of order several microns) about them. The recycling cavity length  $l_r = (l_1 + l_2)/2$  is defined as the average of the optical paths from the recycling mirror to the two arm mirrors, and the Michelson asymmetry  $\Delta l = l_1 - l_2$  is the difference

in these optical paths. At the point  $\delta l_M = 0$  and  $\delta l_r = 0$ , the carrier light interferes destructively at the beamsplitter, sending a minimum of light to the antisymmetric port (the dark fringe condition), and is also resonant in the recycling cavity; thus at this point the carrier power buildup in the interferometer is maximized. The conditions for the RF modulation sidebands are determined by the macroscopic lengths. The modulation frequency  $f_m$  is governed by  $l_r$ ; it is chosen to be equal to the recycling cavity free-spectral-range, in this case  $f_m = c/2/l_r = 25.556\text{MHz}$ . At the carrier dark fringe, the asymmetry  $\Delta l$  results in the modulation sidebands having some finite transmission through the Michelson (from the beamsplitter to the antisymmetric port):

$$t_M = \pm \sin(2\pi f_m \Delta l / c). \quad (2)$$

For maximum transfer of input sideband power to the antisymmetric port,  $t_M$  is chosen (via  $\Delta l$ ) to be approximately equal to the transmission of the recycling mirror,  $t_{RM}$ . With  $\Delta l = 16\text{cm}$  ( $|t_M| = 0.0856$ ), ideally 99% of the input sideband power would be transmitted to the antisymmetric port, but losses in the recycling cavity and mode mismatch reduce this about 70%.

The microscopic lengths naturally fluctuate by of order 1 micron due to seismically driven motion, whereas the operating point defined above must be held within a small fraction of a wavelength of zero (modulo  $\lambda/2$ ). Feedback control is thus used to stabilize the system. The two degrees-of-freedom,  $\delta l_r$  and  $\delta l_M$ , are sensed at the symmetric and antisymmetric ports, respectively. At each port, the light is directed to a photodetector, tuned to have maximum response at  $f_m$  by resonating the diode capacitance with an inductor. Each photodetector output is demodulated at  $f_m$  with a double-balanced diode mixer, to produce a zero-crossing error signal for each degree-of-freedom.

Before writing the equations for the error signals, we define some useful quantities. With  $(r_r, t_r)$  being the field reflectivity and transmission coefficients of the recycling mirror, and  $r_a$  being the average reflectivity of the arm mirrors (including also any loss at the beam splitter), we write the amplitude recycling gains,  $g_{cr}$  (carrier) and  $g_{sb}$  (rf sidebands), the amplitude reflectivity coefficients in reflection,  $r_{cr}$  and  $r_{sb}$ , and the amplitude transmission coefficients to the antisymmetric port,  $t_{cr}$  and  $t_{sb}$ , as

$$\begin{aligned} g_{cr} &= \frac{t_r}{1 - r_r r_a}, & r_{cr} &= \frac{r_r - r_a}{1 - r_r r_a}, \\ g_{sb} &= \frac{t_r}{1 - r_r r_M}, & r_{sb} &= \frac{r_r - r_M}{1 - r_r r_M} \\ t_{cr} &= 0 & \text{and} & \quad t_{sb} = \frac{t_r t_M}{1 - r_r r_M}, \end{aligned} \quad (3)$$

where  $r_M = \sqrt{1 - t_M^2}$ .

For small deviations about the operating point, the signals at the two output ports are

$$\begin{aligned} \frac{S_{\text{anti}}}{S_0} &= g_{cr} t_M k \delta l_M \sin \omega_M t \\ \frac{S_{\text{reff}}}{S_0} &= \left( \frac{g_{cr}^2 r_a r_{sb}}{1 + i \frac{\omega}{\omega_{p1}}} - \frac{g_{sb}^2 r_M r_{cr}}{1 + i \frac{\omega}{\omega_{p2}}} \right) \delta(kl_r) \cos \omega_M t \end{aligned} \quad (4)$$

where  $S_0 = 8J_0(\Gamma)J_1(\Gamma)P_{\text{in}}$ , proportional to the input power  $P_{\text{in}}$ . The reflected port signal is sensitive to the cavity length and the laser frequency,  $\delta(kl_r) = k\delta l_r + 2\pi l_r \delta\nu/c$ , with a response that rolls off according to the carrier ( $\omega_{p1}$ ) and sideband ( $\omega_{p2}$ ) pole frequencies, given by

$$\omega_{p1} = \frac{c}{2l_r} \frac{1 - r_r r_a}{\sqrt{r_r r_a}}, \quad \omega_{p2} = \frac{c}{2l_r} \frac{1 - r_r r_M}{\sqrt{r_r r_M}}. \quad (5)$$

For the parameters in our system, equation 4 results in an equivalent pole frequency for  $S_{\text{reff}}$  at approximately  $\omega_{\text{equiv}} \approx 2\pi \cdot 25\text{kHz}$ .

The feedback for  $S_{\text{anti}}$ , the ‘differential mode’ loop, sends correction signals differentially to the actuators on the two Michelson end mirrors. The loop has a bandwidth of 700 Hz, and reduces differential length fluctuations from 35 nm rms (uncontrolled motion) to  $\sim 0.1$  pm in operation. Maintaining such tight control to the dark fringe is important not only for maximum power build-up, but also to limit the coupling of laser amplitude noise to the output signal (discussed in more detail later).

The feedback for  $S_{\text{reff}}$ , or the ‘common mode’ loop, is more complicated, as it contains the second layer of frequency stabilization (see Fig. 3. Frequency fluctuations of the input light are equivalent to length fluctuations of the recycling cavity; however, they also couple to the output signal through the asymmetry  $\Delta l$ , which makes a frequency dependent phase difference  $\delta\phi$  between the two fields recombining at the beamsplitter:

$$\delta\phi = 2\Delta l \delta k = 4\pi\Delta l \delta\nu/c = 6.7 \times 10^{-9} \text{rad/Hz}. \quad (6)$$

Given our goal phase sensitivity of  $10^{-10} \text{rad}/\sqrt{\text{Hz}}$ , frequency noise must be kept below  $5\text{mHz}/\sqrt{\text{Hz}}$  for it to have an insignificant impact. Since the frequency prestabilization achieves  $0.1\text{Hz}/\sqrt{\text{Hz}}$  at 300 Hz, additional suppression is required from the interferometer itself.

Above 50 Hz, the interferometer mirrors are well isolated from ground vibrations, making an extremely stable frequency reference. At lower frequencies, however, the fractional length fluctuations arising from ground motion (of order  $10^{-6}$ ) exceed the fractional frequency stability of the prestabilized laser beam (of order  $10^{-12} - 10^{-13}$ ). Therefore the control system

is designed to correct both the laser frequency (at high frequencies) and the recycling cavity length (at low frequencies), using two feedback paths. Feedback to the laser is applied to the VCO mentioned above, which drives the AOM to change the laser frequency; feedback to the recycling cavity is applied to the actuators on the recycling mirror. The crossover frequency between these two paths is chosen carefully: the fractional frequency shift available with the VCO is  $10^{-8}$ , much smaller than the low frequency fluctuations of the cavity length, putting an upper constraint on the crossover frequency; on the other hand the need to suppress input frequency fluctuations supplies an upper limit. With  $G_F$  and  $G_L$  being the open loop gain of the laser frequency and recycling cavity length paths, respectively (both being functions of frequency), input laser frequency fluctuations are suppressed by the loop by a factor

$$\frac{1 + G_F + G_L}{1 + G_L}. \quad (7)$$

Thus the suppression is limited by the gain in the length path. To make  $G_L$  sufficiently small above 100 Hz, we operate with the crossover (where  $|G_L| = |G_F|$ ) at 18 Hz, and also include a 100 Hz cut-off, fourth-order low-pass filter in the length path to rapidly reduce  $G_L$  at higher frequencies. The bandwidth of the common mode control is about 50 kHz, with a maximum frequency fluctuation suppression of  $10^3$  from 300-400 Hz.

We also maintain active, interferometric alignment control of the six angular degrees-of-freedom of the interferometer: tip and tilt of the recycling mirror and the two arm mirrors (the beamsplitter orientation is equivalent to a combination of the two arm mirror angles). The sensing is performed with three quadrant photodetectors, each sampling a small fraction of the beam from the symmetric (two detectors) and antisymmetric (one detector) ports. Misalignments produce relative phase gradients between the carrier and rf sideband fields, leading to spatially asymmetric rf amplitude modulation on the light; this amplitude modulation is detected by differencing the outputs of opposing segments of the quadrant detectors[22][23]. These sensor outputs are used in feedback loops to control the orientations of the three interferometer mirrors (i.e., all but the beamsplitter), with control bandwidths of approximately 10 Hz. Uncontrolled alignment fluctuations of order tens of  $\mu\text{radians}$ —which otherwise would reduce the average recycling gain to  $\sim \frac{1}{2}$  its maximum value—are thus suppressed to residual angle errors of  $4\mu\text{radians}$ , approximately 2% of the beam divergence angle.

#### 4. Phase sensitivity

Measurements of the sensing noise were using a dynamic signal analyzer to compute the power spectrum

of the error signal (see Fig. 4). Since the measurement band of interest, 100 Hz to 10 kHz, overlaps the active band of the control loop, the power spectrum is multiplied by  $(1 + G_{\text{diff}})$ , where  $G_{\text{diff}}$  is the open loop gain of the differential mode controls. We also correct for the frequency response of a high-pass filter used to reduce the dynamic range of the signal prior to digitizing. The spectrum is calibrated in terms of equivalent phase difference by applying a known sinusoidal force at 2 kHz to one of the Michelson mirrors, which in turn has been calibrated to mirror displacement using the wavelength-defined fringes of the simple Michelson (recycling mirror misaligned).

Figure 5 shows the measured phase sensitivity spectrum, along with the major broadband noise contributors. Above 600 Hz, the broadband sensitivity is quantum noise limited; i.e., it is determined by the Poisson statistics of photon detection ('shot' noise), at a level of  $(1.28 \pm .04) \times 10^{-10} \text{rad}/\sqrt{\text{Hz}}$ . To our knowledge, this is the best broadband optical phase sensitivity ever demonstrated.

As developed in reference [24], the sensitivity limit due to shot noise in the photodetection for our readout method is:

$$\delta\tilde{\phi}(f) = \sqrt{\frac{2h\nu l}{\eta P_{\text{bs}}}} \cdot \sqrt{(1 + R_a)(1 + \frac{L_c}{t_M^2})} \cdot F_{\text{ns}} \quad (8)$$

where  $h$  is Planck's constant,  $P_{\text{bs}}$  is the carrier power incident on the beam splitter,  $L_c$  is the fraction of  $P_{\text{bs}}$  that is lost at the antisymmetric port due to imperfect interference (the dark fringe not being perfectly dark),  $\eta$  is the photodetector quantum efficiency ( $0.85 \pm 0.03$ ), and  $R_a$  is the ratio of the power in the carrier to that in the sidebands at the antisymmetric output. The first factor in this expression is the idealized phase sensitivity limit for an interferometer with power  $P_{\text{bs}}$  at the beam splitter. The second factor gives the increase in noise due to imperfect interference. The third factor,  $F_{\text{ns}}$ , accounts for the fact that the power at the photodetector is not stationary, but rather has a significant component which varies at  $2f_m$  due to the two rf modulation sidebands[28]. The nonstationary factor  $F_{\text{ns}}$  gives the increase in noise due to the modulation-demodulation scheme, compared to stationary shot noise with the same average photocurrent; it can be expressed in terms of  $R_a$ :  $F_{\text{ns}} = \sqrt{(3/2 + R_a)(1 + R_a)}$ .

We thus can compare our measured noise floor with the shot noise prediction of equation 8. The power at the beam splitter is found by summing the powers in the two beams transmitted through the arm mirrors and correcting for their transmissions, giving  $P_{\text{bs}} = 67 \pm 3 \text{W}$ . The ratio  $R_a$  is found by comparing the DC and  $2f_m$  power levels in a beam sampled from the anti-symmetric port, giving  $R_a = P_{\text{DC}}/(\sqrt{2}P_{2f_m}) - 1 = 1.35 \pm 0.05$ ; the nonstationary factor is thus  $F_{\text{ns}} = 1.10$ . The contrast loss  $L_c$  is found

by operating the interferometer with a much reduced rf modulation index, such that the sideband power at the output is negligible, and measuring the anti-symmetric port power; this results in  $L_c = 2.6 \pm 0.2 \times 10^{-4}$ , making the second factor in equation 8 equal to 1.56. The predicted shot noise sensitivity then comes to  $\delta\tilde{\phi} = (1.36 \pm 0.05) \times 10^{-10} \text{rad}/\sqrt{\text{Hz}}$ , consistent within errors of the measured sensitivity.

We independently verify that the noise floor is dominated by shot noise by separately illuminating the photodetector with a blackbody thermal spectrum, producing the same average photocurrent as in operation. The resulting voltage noise at the readout point is multiplied by the nonstationary factor  $F_{\text{ns}}$ . The resulting spectrum is within 20% of the noise floor of Fig. 5.

It is also interesting to examine the power budget that gives a beam splitter power of 67 W for a carrier input power of  $P_{\text{in}}^c = 0.22 \text{W}$ . This quantities are related by

$$P_{\text{bs}} = P_{\text{in}}^c M \frac{4T_r}{(T_r + L)^2} \quad (9)$$

where  $M$  is the matching efficiency of the input beam to the fundamental cavity mode,  $T_r = t_r^2$ , and  $L$  is the round trip loss in the recycling cavity (less  $T_r$ ). By measuring the resonant reflectivities  $r_{cr}$  and  $r_{sb}$ , we determined that  $M = 0.84$  and  $L = 2 \times 10^{-3}$ , the latter being dominated by the anti-reflection surface of the beam splitter.

In addition to shot noise, there are three broadband noise sources which have non-negligible impact on the sensitivity: beam direction fluctuations, laser frequency noise, and electronics noise.

The Michelson phase difference depends on the input beam direction when the arm mirrors are misaligned (such that either arm mirror does not exactly retro-reflect the beam), because in this case the two arm beams travel different path lengths before recombining at the beam splitter[25][26].

Figure 6 indicates the geometry starting from the beam incident on the beam splitter. The difference in the two paths which start at and return to the beam splitter is:

$$\delta = 2(\Theta_1 - \Theta_2)(y + \bar{l}\Theta_{\text{BS}}) - \Delta l\Theta_{\text{BS}}(\Theta_1 + \Theta_2) + 2\bar{l}(\Theta_1^2 - \Theta_2^2) + \Delta l(\Theta_1^2 + \Theta_2^2 + \Theta_{\text{BS}}^2), \quad (10)$$

where  $\bar{l} = (l_1 + l_2)/2$ . The impact of misalignments is reduced by three effects: the path change is a second order coupling to small lengths ( $y$ ) or angles ( $\Theta_x$ ); the Michelson optics are well isolated, greatly reducing in-band fluctuations of  $\Theta_1$  and  $\Theta_2$ ; fluctuations of the input beam ( $y_{\text{in}}, \Theta_{\text{in}}$ ) are spatially filtered by the recycling cavity. The filtering factor is approximately the power recycling gain, since the TEM<sub>10,01</sub> modes are far off resonance in the recycling cavity. The beam

direction at the beam splitter is related to the input beam directions as:

$$\begin{aligned}\Theta_{\text{BS}} &= 0.97\Theta_{\text{in}}/G_{\text{rec}} = 2.7 \times 10^{-3} \cdot \Theta_{\text{in}} \quad (11) \\ y &= 0.97(y_{\text{in}} + (l_r - \bar{l})\Theta_{\text{in}})/G_{\text{rec}} \\ &= 2.7 \times 10^{-3} \cdot y_{\text{in}} + 1.4 \times 10^{-2} \cdot \Theta_{\text{in}}.\end{aligned}$$

Measurements indicated that the largest effects resulted from the first two terms in equation 10, which involve the input beam direction and motion of the end mirrors. To calibrate the sensitivity, we modulate the angles of the input beam and one of the end mirrors with separate frequencies, and measure the output signal at the sum and difference frequencies. The spectra of the ambient angular motion of the arm mirrors (as measured by the wavefront sensor at the antisymmetric port) and input beam (measured with a quadrant photodetector on the input table) are then convolved and scaled by the measured coupling constant to estimate the contribution to the output signal. Figure 5 shows the result of this procedure; the beam jitter-mirror misalignment contribution is within a factor of 2-3 of the phase sensitivity spectrum in the 110-190 Hz band.

The residual frequency noise contribution is estimated by measuring the error signal of the common mode loop (point **e** in Figure 3). The error signal is converted to frequency units (point **r** in Figure 3) using the 2 kHz calibration peak, and correcting for the gain  $G_L$  in the recycling mirror path. Equation 6 then makes the conversion to equivalent phase noise. While this in-loop measurement is only a lower limit to the frequency noise, it is a good estimate at low frequencies where this noise source is non-negligible.

The largest electronics noise contributors were from the amplifiers that drove the suspended mirror coil actuators in the local damping loops and in the Michelson (differential) feedback control. At worst, electronics noise comes to within a factor of nearly 2 of the measured phase sensitivity, in a small band around 130 Hz.

Two other potential broadband noise sources are laser amplitude noise and thermal noise in the mirrors. Laser noise can couple to the output through the bilinear mechanism implied by equation 4: if the Michelson is not exactly at a dark fringe (i.e.,  $\delta_l \neq 0$ ), either because of an offset or a lack of loop gain, then the output signal  $S_{\text{anti}}$  becomes proportional to the input power. We determined the deviation from dark fringe by applying a known amplitude modulation to the input light and measuring the coupling to the output signal; this gave  $\delta\phi_{\text{rms}} \approx 4\mu\text{radians}$ . Measurements of the beams transmitted by the arm mirrors showed the relative power fluctuations in the recycling cavity to be  $(\delta\langle P \rangle / P) = 3 - 4 \times 10^{-6} / \sqrt{\text{Hz}}$  above 150 Hz. The predicted impact on the phase sensitivity spectrum is thus  $\delta\tilde{\phi} = (\delta\langle P \rangle / P)\delta\phi_{\text{rms}} = 1 - 2 \times 10^{-11} / \text{rad}/\sqrt{\text{Hz}}$ , significantly below the phase

sensitivity. Laser amplitude noise also causes fluctuations of the mirror positions through radiation pressure; if the power incident on the beam splitter is not split evenly between the two arms this technical radiation pressure will cause differential phase noise. In this case, even though the beam splitter is not terribly well-balanced ( $R/T = 51/49\%$ ), technical radiation pressure is estimated to be at an insignificant level of  $\sim 10^{-11} / \text{rad}/\sqrt{\text{Hz}}$  (quantum radiation pressure is lower yet).

Thermally driven fluctuations of the surfaces of the Michelson mirrors and beam splitter must also be considered, an effect governed by the fluctuation-dissipation theorem. Since the beam is much smaller than the mirror diameter, it can be well estimated by the approach of reference [29]. If the internal loss  $\varphi$  of the mirrors is assumed to independent of frequency, the surface fluctuations scale as  $(\varphi/f)^{1/2}$ . For fused silica,  $\varphi$  is generally found to be less than  $10^{-6}$ [30][31][32]; this would produce a phase noise, summing the effect for all three optics, of approximately  $10^{-11} \text{rad}/\sqrt{\text{Hz}}$  at  $f = 100\text{Hz}$ , significantly below the measured phase sensitivity. Even though the quality factors of some of the mirror modes—having modal frequencies  $f > 28\text{kHz}$ —were found to be much less than  $10^6$ , we expect the below-resonance thermal motion is negligible in this measurement.

In addition to these broadband noise sources, there are a variety of periodic or quasi-periodic processes which produce narrow features in the spectrum. The sources of most of these spectral peaks are identified in Figure 7. Several of the peaks were caused by acoustically excited mechanical vibration of components on the input table, producing either beam direction fluctuations or modulation of a scattered light path.

Also evident is thermally driven motion of mechanical modes associated with the suspended Michelson mirrors. The group of peaks around 4 kHz arises from mechanical flexure modes of the actuator magnet assemblies bonded to the mirrors. The peaks at 550 Hz and 1100 Hz correspond to the fundamental and first harmonic modes of the wires used to suspend the mirrors, showing up in the spectrum through the recoil imparted to the optic. For each of these resonances, the amplitude of the spectral peak is consistent with the prediction of a simple model of a resonance driven by thermal energy (Brownian motion):

$$x_{\text{mirror}} \approx \frac{1}{f_0} \sqrt{\frac{k_B T}{\mu}}, \quad (12)$$

where  $f_0$  is the resonance frequency. The reduced mass  $\mu$  for the case of the wire resonances is  $\mu = \frac{1}{2}M(f_n/f_p)^2$ , with  $f_n$  the frequency of the  $n$ th mode,  $f_p$  the frequency of the pendulum mode, and  $M$  the mirror mass; for the magnet assemblies,  $\mu = M^2/m$ , with  $m$  the magnet assembly mass (700 mg). The

thermal noise above and below the peaks can be estimated using the fluctuation-dissipation theorem, following the approach of reference [27]; we assume the resonances are structurally damped, with a loss of  $10^{-4}$  and  $10^{-2}$  for the wire and magnet assembly resonances, respectively (the loss numbers derive from the peak widths seen in a high resolution spectrum). Neither type of mode creates significant off-resonance thermal noise.

## 5. Power limitations

With the available laser power, the interferometer could operate up to a circulating power level of 120 W, but the best sensitivity was achieved at about 70 W of power in the recycling cavity. At higher power, the system suffered from increasing optical distortion caused by absorption in the optics, an issue which has long been a concern for gravitational wave interferometers given the high powers required for good sensitivity[33]. Energy absorbed in the optics, either through bulk substrate or surface absorption, heats the material and can produce both thermoelastic surface distortions and ‘thermal lens’ distortions via the temperature dependence of the index of refraction (important for transmissive elements). In fused silica, thermal lensing is the dominant effect, implying that in this experiment the beam splitter is the critical element. Absorption in the beam splitter primarily affects the contrast of the Michelson, since the thermal lensing acts on only one of the arms. We investigated this effect by measuring the Michelson contrast loss  $L_c$  as a function of the power on the beamsplitter (Fig. 8, varying the input power and reducing the modulation depth such that there was insignificant rf sideband power at the anti-symmetric port.

At very low power, thermal distortions are insignificant and the loss is dominated by the effect of the asymmetry  $\Delta l$ , which leads to a mismatch of gaussian parameters of the two beams recombining on the beam splitter (the mismatch is primarily in their wavefront curvatures)[34]. As the power increases, the beam splitter heats up and begins to act as a lens for the beam traversing the substrate. The initial lensing actually improves the matching of the two beams and lowers the contrast loss—the positive  $dn/dT$  of fused silica compensates for the longer physical path length of the arm containing the beam splitter substrate (the compensation is not perfect—the thermal lens deviates from cylindrical symmetry because the beam travels at an angle through the substrate). As the power is further increased, the lensing overwhelms the asymmetry and the contrast loss increases.

With increasing contrast loss, at some point the shot noise increases more quickly than the signal sensitivity  $S_{\text{anti}}$ , and the signal-to-shot-noise ratio decreases. The best noise performance was obtained with an input carrier power of 210 mW, for which  $P_{\text{bs}} = 67\text{W}$ . We note that in LIGO, the beam split-

ter substrate is a lower-loss grade of fused silica; the fractional bulk absorption is expected to be approximately  $5\times$  smaller than estimated here, so that LIGO can operate with 200 W on the beam splitter.

## 6. Conclusion

The results of this prototype are close to the required LIGO phase sensitivity. The sensitivity is quantum noise limited above 600 Hz; the optical power which determines this sensitivity was limited not by available laser power, but by thermal loading in the beam splitter. The most dramatic difference between this work and the previous version of this experiment[11] is the large sensitivity improvement below 1.5kHz. This is primarily the result of better frequency stabilization and more effective control of scattered light.

The sources of much of the broadband excess noise below 500 Hz has been identified. The quadrature sum of the known noise sources is within 50% of the measured noise everywhere above 150 Hz. The quadrature difference between the measured and the known noise terms has approximately a  $1/f^{3/2}$  spectrum, though the source(s) of this noise have not been identified.

## 7. Acknowledgements

We thank the entire LIGO team at Caltech and MIT for assistance and support. This work was supported by National Science Foundation Grant PHY-9210038.

## References

1. R. Weiss, “Electromagnetically coupled broadband gravitational antenna,” MIT Res. Lab. Electron. Q. Prog. Rep. **105**, 54–76 (1972).
2. See, for example, K.S. Thorne, “Gravitational radiation,” in *300 Years of Gravitation*, S.W. Hawking and W. Israel, eds. (Cambridge U. Press, Cambridge, UK, 1987), pp. 330–458.
3. Ke-Xun Sun, M.M. Fejer, E. Gustafson, and R.L. Byer, “Sagnac Interferometer for Gravitational-Wave Detection,” Phys. Rev. Lett. **76**, 3053–3056 (1996).
4. A. Abramovici, B. Althouse, R. Drever, Y. Gursel, S. Kawamura, F. Raab, D. Shoemaker, L. Sievers, R. Spero, K. Thorne, R. Vogt, R. Weiss, S. Whitcomb, M. Zucker, “LIGO: The Laser Interferometer Gravitational-Wave Observatory,” Science **256** 325–333 (1992).
5. B. Caron, A. Dominjon, C. Drezen, R. Flaminio, X. Grave, F. Marion, L. Massonnet, C. Mehmel, R. Morand, B. Mours, V. Sannibale, M. Yvert, D. Babusci, S. Bellucci, S. Candusso, G. Giordano, G. Matone, J.-M. Mackowski, L. Pinard, F. Barone, E. Calloni, L. DiFiore, M. Flagiello, F. Garuti, A. Grado, M. Longo, M. Lops, S. Marano, L. Milano, S. Solimeno, V. Brisson, F. Cavalier, M. Davier, P. Hello, P. Heusse, P. Mann, Y. Acker, M. Barsuglia, B. Bhawal, F. Bondu, A. Brillet, H. Heitmann, J.-M. Innocent, L. Latrach, C.N. Man, M. PhamTu, E. Tournier, M. Taubmann, J.-Y. Vinet, C. Boccara, P. Gleyzes, V. Lorette, J.-P. Roger, G. Cagnoli, L. Gammaitoni, J. Kovalik, F. Marchesoni, M. Punturo, M. Beccaria, M. Bernardini, E. Bougleux, S. Braccini, C. Bradaschia, G. Cella, A. Ciampa, E. Cuoco, G. Curci, R. DelFabbro, R. DeSalvo, A. DiVirgilio, D. Enard, I. Ferrante, F. Fidecaro, A. Giassi, A. Giazotto, L. Holloway, P. LaPenna, G. Losurdo, S. Mancini, M. Mazzoni, F. Palla, H.-B. Pan, D. Passuello, P. Pelfer, R. Poggiani, R. Stanga, A. Vicere, Z. Zhang, V. Ferrari, E. Majorana, P. Puppò, P. Rapagnani, and F. Ricci, “The VIRGO interferometer for gravitational wave detection,” Nucl. Phys. **B54**, 167–175 (1997).
6. K. Danzmann, “GEO 600 — A 600-m Laser Interferometric Gravitational Wave Antenna,” in *First Edoardo Amaldi conference on gravitational wave experiments*, E. Coccia, G. Pizella and F. Ronga, eds. (World Scientific, Singapore, 1995), p. 100–111.
7. K. Tsubono, “300-m Laser Interferometer Gravitational Wave Detector (TAMA300) in Japan,” in *First Edoardo Amaldi conference on gravitational wave experiments*, E. Coccia, G. Pizella and F. Ronga, eds. (World Scientific, Singapore, 1995), p. 112–114.
8. D. Shoemaker, R. Schilling, L. Schnupp, W. Winkler, K. Maischberger, and A. Rüdiger, “Noise behavior of the Garching 30-meter prototype gravitational-wave detector,” Phys. Rev. D **38**, 423-432 (1988).
9. Robert Forward, “Wideband laser-interferometer gravitational-radiation experiment,” Phys. Rev. D **17**, 379-390 (1978).
10. Gerald Blum and Rainier Weiss, “Experimental Test of the Freundlich Red-Shift Hypothesis,” *Physical Review*, **155**, 1412-1413 (1967).
11. P. Fritschel, G. González, B. Lantz, P. Saha, and M. Zucker, “High Power Interferometric Phase Measurement Limited by Quantum Noise and Application to Detection of Gravitational Waves,” Phys. Rev. Lett. **80**, 3181-3184 (1998).
12. A. Abramovici, W. Althouse, J. Camp, J.A. Giaime, A. Gillespie, S. Kawamura, A. Kuhnert, T. Lyons, F.J. Raab, R.L. Savage Jr., D. Shoemaker, L. Sievers, R. Spero, R. Vogt, R. Weiss, S. Whitcomb, and M. Zucker, “Improved sensitivity in a gravitational wave interferometer and implications for LIGO,” Phys. Lett. **A218**, 157–163 (1996).
13. R.W.P. Drever, J. Hough, A.J. Munley, S.A. Lee, R. Spero, S.E. Whitcomb, H. Ward, G.M. Ford, M. Hereld, N.A. Robertson, I. Kerr, J.R. Pugh, G.P. Newton, B. Meers, E.D. Brook III, and Y. Gursel, “Gravitational wave detectors using laser interferometers and optical cavities,” in *Quantum Optics, Experimental Gravity, and Measurement Theory*, P. Meystre and M.O. Scully, eds. (Plenum, New York, 1983), pp. 503–524.
14. H. Billing, K. Maischberger, A. Rüdiger, R. Schilling, L. Schnupp, and W. Winkler, “The Munich Gravitational Wave Detector using laser interferometry,” *ibid*, pp. 525–566.

15. L. Schnupp, Max Planck Institute for Quantum Optics, Garching, Germany (private communication, 1986).
16. R.L. Savage Jr., P.J. King, and S.U. Seel, "A Highly Stabilized 10-Watt Nd:YAG Laser for the Laser Interferometer Gravitational Wave Observatory (LIGO)," *Laser Physics*, **8**, 679–685 (1998).
17. R.W.P. Drever, J.L. Hall, F.V. Kowalski, J. Hough, G.M. Ford, A.J. Munley, and H. Ward, "Laser phase and frequency stabilization using an optical resonator," *Appl. Phys.* **B31**, 97–105 (1983).
18. STACIS, Technical Manufacturing Company, 15 Centennial Drive, Peabody, MA.
19. J. Giaime, P. Saha, D. Shoemaker, and L. Sievers, "A passive vibration isolation stack for LIGO: design, modeling, and testing," *Rev. Sci. Instrum.* **67**, 208–214 (1996).
20. R. Schilling, L. Schnupp, W. Winkler, H. Billing, K. Maischberger, and A. Rüdiger, "A method to blot out scattered light effects and its application to a gravitational wave detector," *J. Phys. E:Sci. Instrum.* **14** 65–70 (1981).
21. The photodiode is 2mm diameter InGaAs, model C30642G from EG&G Optoelectronics, operated without the protective window. The beam impinges on the diode at a 30 deg angle-of-incidence to control the specular reflection; at this angle we have measured its backscattering to be  $3.7 \times 10^{-5}$ /steradian.
22. E. Morrison, B.J. Meers, D.I. Robertson, and H. Ward, "Automatic alignment of optical interferometers," *Appl. Opt.* **33**, 5041-5049 (1994).
23. Y. Hefetz, N. Mavalvala, D. Sigg, "Principles of Calculating Alignment Signals in Complex Resonant Optical Interferometers," *J. Opt. Soc. Am. B* **14** 1597–1605 (1997).
24. B. Lantz, Ph.D. thesis, Massachusetts Institute of Technology, 1999.
25. P. Saha, Ph.D. thesis, Massachusetts Institute of Technology, 1997.
26. A. Rüdiger, R. Schilling, L. Schnupp, W. Winkler, H. Billing, and K. Maischberger, "A mode selector to suppress fluctuations in laser beam geometry," *Optica Acta* **28** 641–658 (1981).
27. P. Saulson, "Thermal noise in mechanical experiments" *Phys. Rev. D* **42**, 2437-2445 (1990).
28. T.M. Neibauer, R. Schilling, K. Danzmann, A. Rüdiger, W. Winkler, "Nonstationary shot noise and its effect on the sensitivity of interferometers," *Phys. Rev. A* **43**, 5022–5029 (1991).
29. Yu. Levin, "Internal thermal noise in the LIGO test masses: A direct approach," *Phys. Rev. D* **57**, 659–663 (1998).
30. W.J. Startin, M.A. Bielby, P.R. Saulson, "Mechanical quality factors of fused silica resonators," *Rev. Sci. Instr.* **69**, 3681-3689 (1998).
31. B.S. Lunin, S.N. Torbin, M.N. Danachevskaya, I.V. Batov, Transl. D.D. Lynch, *Bulletin of Moscow State University, Series 2, Chemistry* **35**, 24-28 (1994).
32. S. Rowan, S.M. Twyford, J. Hough, D. Gwo, R. Route, "Mechanical losses associated with the technique of hydroxide-catalysis bonding of fused silica," *Phys. Lett. A* **246**, 471-478 (1998).
33. W. Winkler, K. Danzmann, A. Rüdiger, and R. Schilling, "Heating by optical absorption and the performance of interferometric gravitational-wave detectors," *Phys. Rev. A* **44**, 7022-7036 (1991).
34. The mirror surface distortions and beam splitter substrate inhomogeneities contributed insignificantly to the contrast loss; this was clear not only because the calculated asymmetry loss matched the measured loss, but also because the spatial distribution of the anti-symmetric port beam had the cylindrical symmetry expected for this effect.

Table 1. Significant parameters of the interferometer.

Parameter	Value
Mirror diameter $\times$ thickness	76.2mm $\times$ 25.4mm
Recycling mirror transmission; radius of curvature	0.63%; 10 m concave
Recycling cavity length, $l_r$	5.87 m
Michelson asymmetry, $\Delta l$	0.16 m
Recycling mirror–beam splitter separation	5.37 m
Beam waist size, $\omega_0$	1.30 mm
Arm mirror transmission	7.4 ppm
Modulation frequency; depth	25.556 MHz; 0.4 rad
Mode matching efficiency	85%
Recycling gain, $G_{rec}$	365

Fig. 1. Amplitude spectra of the phase sensitivity of various instruments. Shown along with the results of this experiment are the sensitivities of: the initial LIGO interferometers[4]; three previous prototype gravitational wave interferometers—Fritschel et al.[11](the precursor to this experiment); Shoemaker et al.[8] and Forward[9]; and an interferometric test of the Freundlich red shift hypothesis[10]

Fig. 2. Schematic of the instrument. All components within the vacuum enclosure are mounted on seismically isolated platforms, with the four interferometer optics mounted as pendula. The recycling cavity length is  $l_r = (l_1 + l_2)/2$  and the Michelson asymmetry is  $\Delta l = l_1 - l_2$ . Other symbols are as follows: VCO: voltage-controlled oscillator; A: acousto-optic modulator; C: circulator; RM: recycling mirror; BS: beam splitter; CM: common mode; DM: differential mode;  $C_P$ : frequency prestabilization control;  $C_F$ : common mode servo frequency control;  $C_L$ : common mode servo length control;  $C_{diff}$ : differential mode control.

Fig. 3. Block diagram of the common mode control system. **D** represents the frequency detection, and converts frequency to voltage;  $C_L$  is the compensation for the length control path, and converts voltage to displacement of the recycling mirror;  $C_F$  is the compensation for the frequency control path, and converts voltage to input light frequency; **H** converts displacement of the recycling mirror to resonant frequency of the recycling cavity. The loop gain in the length and frequency paths is  $G_L = DC_L H$  and  $G_F = DC_F$ , respectively.

Fig. 4. Differential mode readout and control. The light is detected with an InGaAs photodiode and associated preamp (most of the power at this port is modulated at  $2f_m$ , which is notched out before the preamp to avoid saturation). The photodetector output is demodulated to provide the output signal, measured through a high-pass filter to reduce the dynamic range of the signal. The demodulator signal is also sent through the feedback control  $C_{diff}$  to maintain the Michelson on the carrier dark fringe. The 2kHz calibration is a known force applied to one of the arm mirrors.

Fig. 5. The measured phase sensitivity spectrum (top curve), along with the estimated contributions from several noise sources: residual frequency noise; electronics noise in the mirror actuator amplifiers; beam direction fluctuations (beam jitter); thermal noise in the magnet-actuators bonded to the mirrors (fin thermal). The root-square-sum of these identified noise sources is also shown.

Fig. 6. Distances and angles in the misaligned interferometer.

Fig. 7. Identification of narrow spectral features.

Fig. 8. Fractional contrast loss (ratio of antisymmetric port power to beam splitter power) as a function of power on the beam splitter. The loss at very low power is due to the beam mismatch arising from the Michelson asymmetry. This is nearly cancelled by the thermal lens in the beam splitter at about 55 W; for higher powers the thermal lens dominates and increases the loss quadratically.

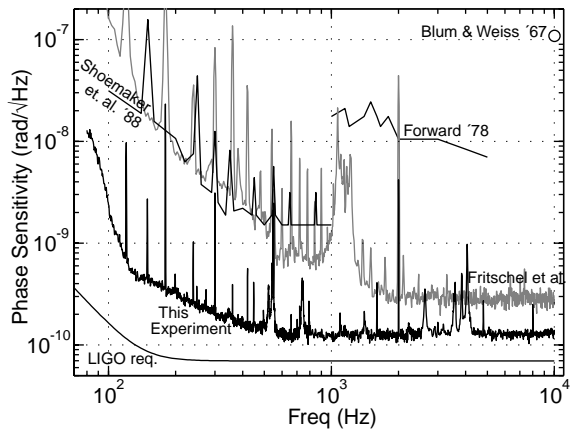


Figure 1, Brian Lantz et al.

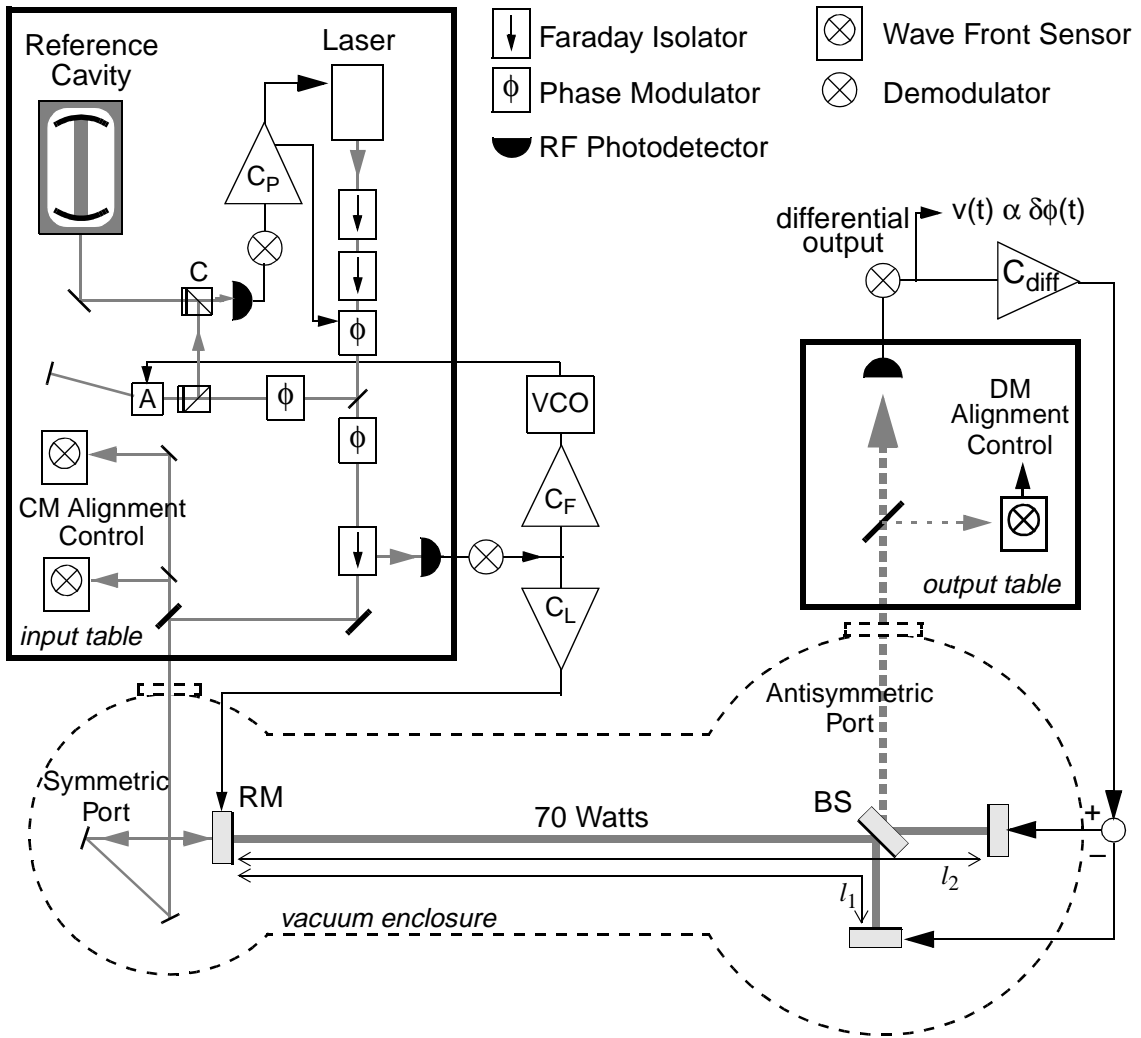


Figure 2, Brian Lantz et al.

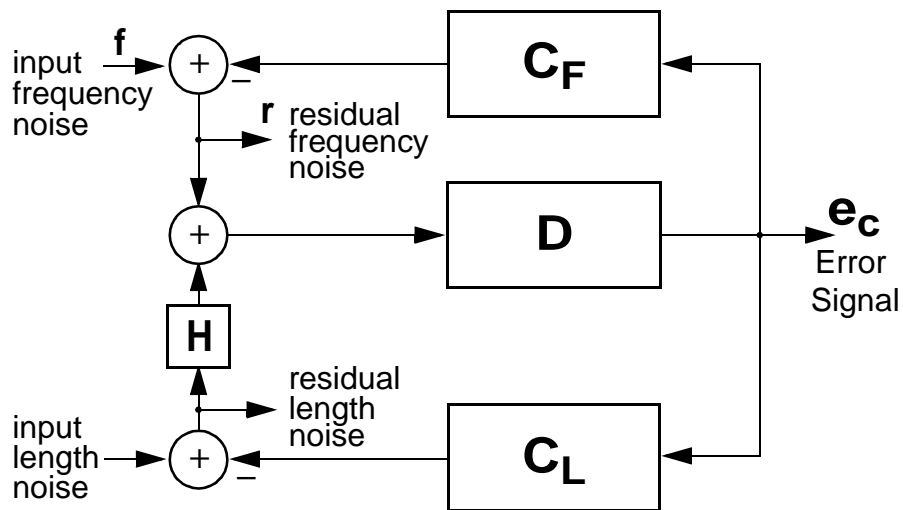


Figure 3, Brian Lantz et al.

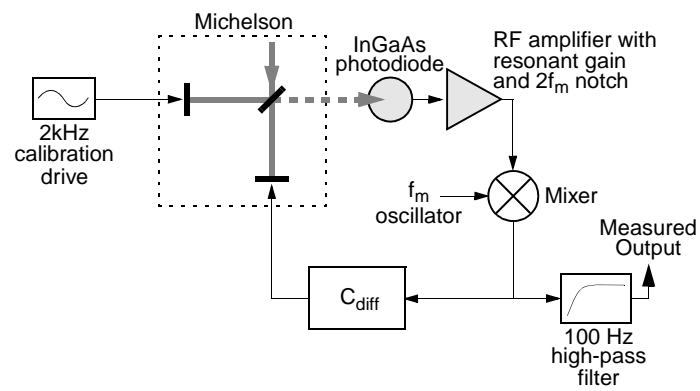


Figure 4, Brian Lantz et al.

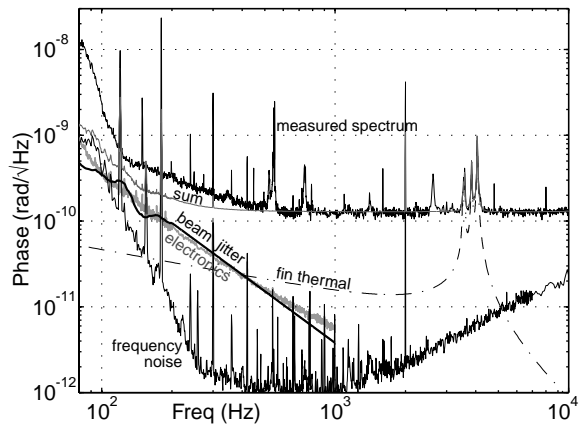


Figure 5, Brian Lantz et al.

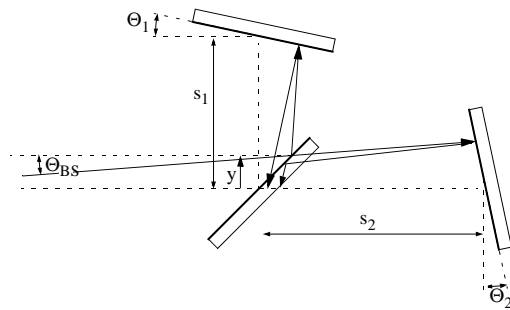


Figure 6, Brian Lantz et al.

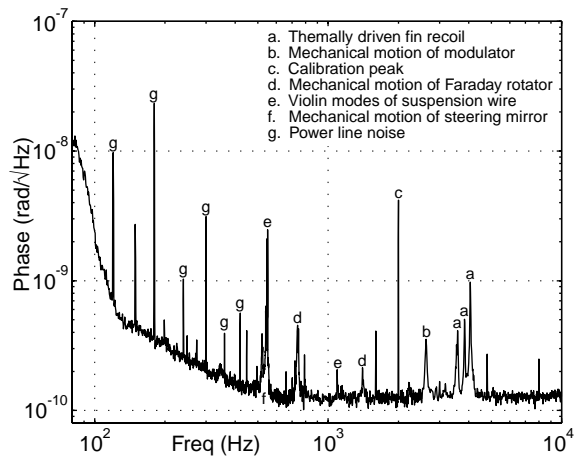


Figure 7, Brian Lantz et al.

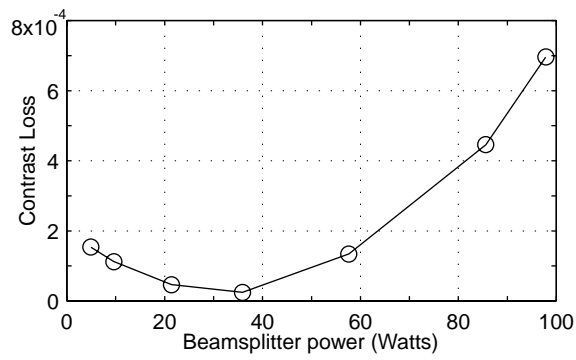


Figure 8, Brian Lantz et al.